Three-dimensional laser microvision

Hiroshi Shimotahira, Keigo Iizuka, Sun-Chun Chu, Christopher Wah, Fumie Costen, and Yuzo Yoshikuni

A three-dimensional (3-D) optical imaging system offering high resolution in all three dimensions, requiring minimum manipulation and capable of real-time operation, is presented. The system derives its capabilities from use of the superstructure grating laser source in the implementation of a laser step frequency radar for depth information acquisition. A synthetic aperture radar technique was also used to further enhance its lateral resolution as well as extend the depth of focus. High-speed operation was made possible by a dual computer system consisting of a host and a remote microcomputer supported by a dual-channel Small Computer System Interface parallel data transfer system. The system is capable of operating near real time. The 3-D display of a tunneling diode, a microwave integrated circuit, and a see-through image taken by the system operating near real time are included. The depth resolution is 40 μm; lateral resolution with a synthetic aperture approach is a fraction of a micrometer and that without it is approximately 10 μm. © 2001 Optical Society of America

OCIS codes: 100.0100, 100.0200, 100.6740, 100.6890, 100.3080, 120.4640.

1. Introduction

As integrated optical circuits become finer and more intricate, the necessity for a high-resolution, fast-acquisition time fault locator increases. We propose a new imaging device named the three-dimensional (3-D) Laser Microvision. This device has the ability of providing a 3-D see-through image of microstructured objects with minimum necessity of manipulation and with a long focal depth within a reasonable time. It can have many applications, for example, as a diagnostic tool for the optical integrated circuits (IC's), a noncontact surface deposition monitor, or a device to see through the opaque cover of the IC's.

There are certainly other devices that currently exist, but they all have their own advantages and disadvantages, and a specific choice would depend on the specific application. An optical time-domain reflectometer[1,2] is the most commercially successful device as a fault locator of an optical fiber. Its spatial resolution is at most a few meters, and as the required resolution becomes higher, more complicated apparatuses are needed to generate and detect a short optical pulse. A frequency-domain reflectometer[3,4] has been proposed to obtain higher resolution with reasonable cost. Use of discrete Fourier analysis techniques has given rise to the step frequency method.[5,6]

The optical coherence-domain reflectometer[7] is another successful device, especially in medical diagnosis. This device is, in principle, a Michelson interferometer with a variable reference path length. The simplicity of the system and micrometer-order resolution are excellent; however, operation speed and measurable range are limited because of the existence of the mechanical part to sweep the reference path length. An optical coherence-domain reflectometer by synthesis of the coherence function,[8] which has no mechanical moving part, was proposed to overcome these difficulties. Recently, in this approach, a superstructure grating (SSG) distributed Bragg reflector (DBR) laser diode was adopted, and its application to tomography for scattering media was reported.[9]

For a given wavelength of light, the diffraction limit imposes a barrier on the ultimate lateral resolution that is achievable by an imaging system rely-

When this research was performed, the authors were with Advanced Telecommunication Research of Japan, 2-2 Hikaridai Seika-cho, Soraku-gun, Kyoto 612-02, Japan. H. Shimotahira is now with the Anritsu Corporation, 1800 Onna, Atsugi-shi, Kanagawa Prefecture 243-8555, Japan. K. Iizuka (keigo.iizuka@utoronto.ca), S.-C. Chu, and C. Wah are now with the Department of Electrical and Computer Engineering, University of Toronto, Toronto, Ontario M5S 1A4, Canada. F. Costen is now with the Department of Computer Science, University of Manchester, Manchester, United Kingdom. Y. Yoshikuni is now with NTT Opto-electronics Laboratories, Atsugi-shi 243-01, Japan.

Received 3 January 2000; revised manuscript received 10 October 2000.

0003-6935/01/111784-11$15.00/0

ing on the collection of far-field information. To achieve higher resolution, a shorter wavelength source such as that employed by the scanning electron microscope[10] is used. This limit, however, can be breached if near-field information is collected and used. The scanning near-field optical microscope[11] is such a device that employs a small pinhole probe to collect optical fields found close to the target. There are many other devices for nanostructured objects, such as the electron[12] or photon[13] tunneling microscope and the atomic force microscope.[14] Nanometer-order resolution is definitely attractive, but in these devices the setting up of both the objects and the apparatus is critical, and most of them can see only the surface profile of the objects.

The advantages of the 3-D Laser Microvision compared with the above-mentioned devices are manifold. One is the capability of generating a 3-D image of the sample that has a resolution of the order of micrometers. A 3-D image rather than a two-dimensional (2-D) image significantly increases the information on the topology of the sample as well as the maneuverability of the operator analyzing the sample. Another advantage is that when the 3-D Laser Microvision is used to locate the faults in an optical guide in an integrated optics wafer, not only the location but also the amount of the scattered light can be known immediately. If, for example, the scanning electron microscope were used for the same purpose, the amount of the reflected light would have to be determined by other means.

In this paper we first show the principle of operation of the 3-D Laser Microvision. The longitudinal (depth) and lateral resolutions of this device are studied, and a synthetic aperture approach to improve the lateral resolution is proposed. The result of computer simulations to investigate the optimum conditions in setting up this approach are also given. Then specially developed hardware and software for real-time operation are presented. Finally, we show some displays of the 3-D Laser Microvision when a photodiode on a GaAs substrate, a V groove on a Si wafer, etc., are used as a target, and we prove its capability of providing a 3-D see-through image of the target and its applicability as a diagnostic tool for optical IC's.

2. Principle of Operation

The proposed 3-D Laser Microvision is based on the principle of a step frequency radar. Optically, it is an interferometer that determines the distance from the information of the phase delay of the scattered signal. Figure 1 shows the layout of the 3-D Laser Microvision. The carrier frequency of the SSG laser diode[15,16] is swept stepwise. In each step of frequency, the following procedure is repeated. The output laser light is split into the probe and reference beams by means of an acousto-optic modulator (AOM). The nonrefracted beam (the zeroth-order beam) from the AOM is used as a probe beam, and the refracted beam (the first-order beam) from the AOM whose carrier frequency is

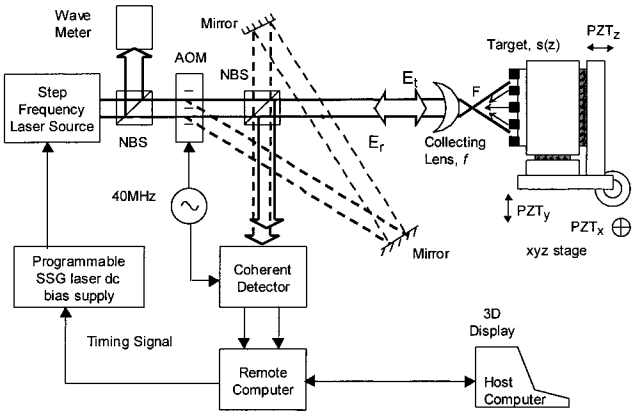

Fig. 1. Block diagram of the 3-D Laser Microvision. NBS, nonpolarizing beam splitter; AOM, acousto-optic modulator; PZT, piezoelectric transducer.

shifted from that of the probe beam by the frequency of excitation of the AOM is used as a local oscillator beam. The probe beam reflected from the target is mixed with the reference beam from the AOM in a coherent detector and heterodyne-detected signal, both amplitude and phase, and is stored in a computer. The heterodyne detection not only makes phase detection simpler but also improves the signal-to-noise ratio of the system. After all stepping of the frequencies are finished, the stored data are processed by the computer and a 3-D image of the target is displayed.

The wavelength of the SSG laser diode is centered at 1.545 μm, and this value would be suitable for use in semiconductor wafers. A quantum of 1.5-μm wavelength light is $h\nu = 0.83$ eV. Semiconductors with a bandgap wider than 0.83 eV are transparent to this wavelength light because the light cannot generate electron–hole pairs. Thus both Si ($h\nu = 1.1$ eV) or GaAs ($h\nu = 1.4$ eV) wafers are transparent to the probe beam, and one can easily obtain the see-through image of optical IC's fabricated on semiconductor wafers.

By the above-mentioned method, frequency stepping and probe-beam-focusing characteristics determine the longitudinal (depth) and lateral resolutions, respectively. Next we study each resolution in detail.

A. Longitudinal (depth) Resolution

The theory used for the longitudinal distance discrimination is essentially the same as that described in Ref. 4, but a shortened version is repeated here because we use these formulas to discuss the design of the system, expected resolution, and range of the device, as well as to provide an appreciation of the experimentally obtained results. For simplicity, we suppose that all scatterers are localized at discrete points $z_m = z_0 + m\Delta z$, where $m = 0, 1, \ldots, N - 1$. Our aim is to find the scattering coefficients at $z = z_m$, which is denoted as $s(z_m)$. When we send a cw light of carrier frequency $f_n = f_0 + n\Delta f$, which is the fre-

quency at the nth step, the received signal $S(f_n)$ without an inessential coefficient is given as follows,

$$S(f_n) = \sum_{m=0}^{N-1} s(z_m)\exp\left[j\frac{4\pi}{v}(f_0 + n\Delta f)(z_0 + m\Delta z)\right]$$
$$= \exp\left(j\frac{4\pi}{v}f_n z_0\right)\sum_{m=0}^{N-1} s(z_m)\exp\left(j\frac{4\pi}{v}f_0 m\Delta z\right)$$
$$\times \exp\left(j\frac{4\pi}{v}mn\Delta f\Delta z\right), \quad (1)$$

where v is the velocity of light. If we let

$$H(n) = S(f_n)\exp\left(-j\frac{4\pi}{v}f_n z_0\right), \quad (2)$$

$$h(m) = Ns(z_m)\exp\left(j\frac{4\pi}{v}f_0 m\Delta z\right), \quad (3)$$

$$\frac{2\Delta f\Delta z}{v} = \frac{1}{N}, \quad (4)$$

then Eq. (1) becomes

$$H(n) = \frac{1}{N}\sum_{m=0}^{N-1} h(m)\exp\left(j\frac{2\pi nm}{N}\right). \quad (5)$$

Equation (5) is in the form of an inverse discrete Fourier transform (DFT). Taking the DFT on both sides of Eq. (5), we obtain

$$h(m) = \sum_{n=0}^{N-1} H(n)\exp\left(-j\frac{2\pi mn}{N}\right). \quad (6)$$

Therefore $h(m)$ and $H(n)$ form a DFT pair under the necessary condition stated in Eq. (4). In practice, a fast Fourier transform (FFT) has been used in place of the DFT to speed up the processing time. There are several important properties concerning this relationship that are worth mentioning. First, from Eq. (4) the total frequency span $N\Delta f$ and the frequency step Δf determine the depth resolution Δz and measurable range $z_{\max}$; the respective expressions are given as follows:

$$\Delta z = \frac{v}{2N\Delta f}, \qquad z_{\max} = N\Delta z = \frac{v}{2\Delta f}. \quad (7)$$

According to Eq. (6), $H(n)$ is the function that fed into the FFT processor. However, it is clear from Eq. (2) that $H(n)$ is different from what is actually measured by the coherent detector. It is therefore important to relate $H(n)$ to the physically measured quantities $S(f_n)$ so that $H(n)$ can be constructed for FFT processing. From Eq. (2),

$$\|H(n)\| = \|S(f_n)\|, \quad (8)$$

$$\arg[H(n)] = \arg[S(f_n)] - \frac{4\pi}{v}(f_0 + n\Delta f)z_0. \quad (9)$$

Equation (8) states that the magnitudes of $H(n)$ and $S(f_n)$ are equal. Therefore no preprocessing is needed to construct $\|H(n)\|$. Similarly, from Eq. (9), $\arg[S(f_n)]$ is the phase that is physically measured. It is different from $H(n)$ by $[4\pi/v(f_0 + n\Delta f)z_0]$ rad. Therefore $\arg[S(f_n)]$ must be subtracted by this phase correction factor to obtain the phase of $H(n)$. This phase correction factor is nothing but the phase delay that is due to the path difference introduced by the target at z_0. In practice, we can obtain this correction factor by placing a target at a predetermined distance. Phases of all frequency steps are taken and stored in the computer memory for later subtraction. The technique mentioned above also serves to correct phase errors that are introduced in the system.

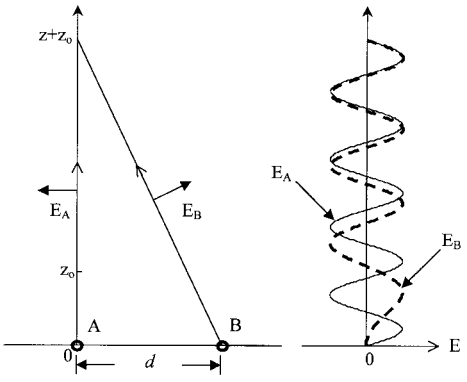

Fig. 2. Principle of the synthetic aperture 3-D Laser Microvision.

Last, according to Eq. (3),

$$\|s(z_m)\| = \frac{1}{N}\|h(m)\|; \quad (10)$$

therefore we can obtain $\|s(z_m)\|$, the magnitude of the scattering coefficient, by multiplying the scaling factor $1/N$ to $\|h(m)\|$.

B. Lateral ($x - y$ plane) Resolution

So far we have obtained the lateral resolution (x–y plane resolution) from focusing the objective lens, and it is best only at one focused depth. To remove this difficulty, the synthetic aperture 3-D Laser Microvision is proposed. The synthetic aperture approach comes from that of the microwave Side-Looking Airborne Radar,[17] which makes high-resolution maps from scanned microwave echoes. A linear flight path of an airplane is used as a linear scan path of the probing antenna. With the 3-D Laser Microvision the light scattered from the target is measured as the probe is moved away from the target along a path perpendicular to the surface of the target. Thus the scanned probe collects information about the scatterer and significantly improves the lateral resolution as well as the depth resolution of the 3-D Laser Microvision.

The principle of the synthetic aperture 3-D Laser Microvision is shown in Fig. 2. Let us suppose that there are only two point targets side by side. Point A at (0, 0, 0) is the desired target and point B at (d, 0, 0) is a disturber. The probe is scanned along the z

axis, and the contributions that are due to both A and B are received. The field that is due to point A is

$$E_A(z) = A \exp\left(j \frac{2\pi}{\lambda} z\right) = A \exp(j2\pi f_s z). \quad (11)$$

The phase of $E_A(z)$ linearly increases with z with spatial frequency $f_s = 1/\lambda$. In contrast, the field that is due to point B is

$$E_B(z) = B \exp\left[j \frac{2\pi}{\lambda} (z^2 + d^2)^{1/2}\right]. \quad (12)$$

If $z^2 > d^2$, the phase of $E_B(z)$ can be approximated as

$$\phi = \frac{2\pi}{\lambda}\left(z + \frac{d^2}{2z}\right). \quad (13)$$

Note that now the spatial frequency of the contribution from point A is f_s whereas that from point B is smaller than that by $f_s \times (d^2/2z^2)$. In general, the spatial frequency associated with the target point that is exactly underneath the scan is always the highest. With the Fourier transform, that is, by calculation of the Fourier coefficient,

$$\int_{z_0}^{z_0+z} E(z')\exp(-j2\pi f_s z')\mathrm{d}z', \quad (14)$$

where $E(z')$ is the field measured at z'. Note that only the spectrum with f_s needs to be calculated, and we need not calculate the entire FFT spectrum. Next we study the optimum conditions about the starting point z_0 and the scanning distance z.

C. Optimum Conditions in the Near-Field Synthetic Aperture Approach

The optimum choice of the combination of the starting and ending points of the vertical scan in the synthetic aperture approach was examined by computer simulation. The target is moved along the z axis. The point at $z = 0$ in this coordinate system corresponds to the focal point of the focusing lens of the probe beam in our experimental system shown in Fig. 1. Figure 2 shows only the necessary coordinate system used for the computer simulation. Suppose that the desired target A is located at the $(x, y) = (0, 0)$, whereas the disturber B is at (5.0 μm, 0).

At first the starting point of the vertical scan that is denoted as z_0 is taken as a parameter. When z_0 is set to be 2, 5, and 10 μm, the resulting intensity of the Fourier transform of the detector output with respect to the spatial frequency is shown in Figs. 3(a), 3(b), and 3(c), respectively. The scanning distance is fixed at 10 μm. In each graph, the spectral curves for the desired target (solid curve) and the disturber (dashed curve) alone are plotted. The ratio between the spectral intensities that are due to the target and the disturber alone at $f_s = 0.66 = 1/1.5\ \mu\mathrm{m}^{-1}$ is defined as the signal-to-interference ratio (SIR). The SIR is expressed as follows and is used as an indicator of the performance of the synthetic aperture approach:

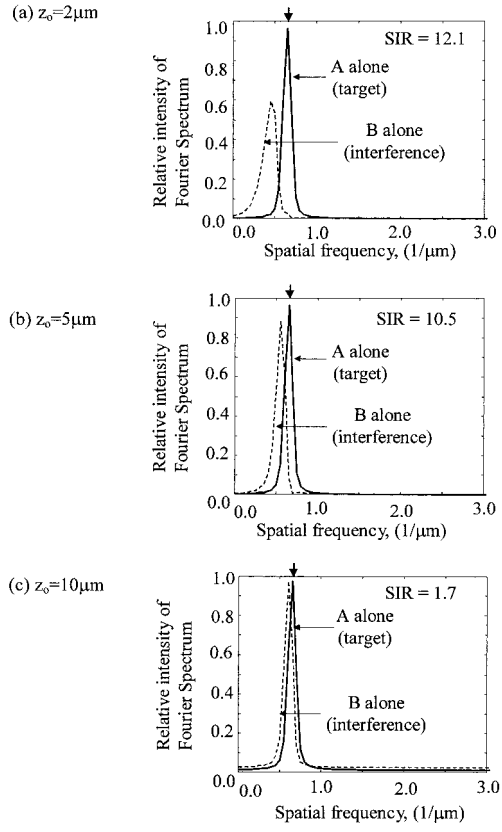

Fig. 3. Fourier transform of the detector output with respect to the distance z of the vertical scan. The scan distance is $z = 10$ μm. The top arrow indicates the location of the spatial frequency of interest. (a) $z_0 = 2$ μm, (b) $z_0 = 5$ μm, and (c) $z_0 = 10$ μm.

$$\mathrm{SIR} = \left|\frac{\int_{z_0}^{z_0+z} E_A(z')\exp(-j2\pi f_s z')\mathrm{d}z'}{\int_{z_0}^{z_0+z} E_B(z')\exp(-j2\pi f_s z')\mathrm{d}z'}\right|^2 = \left|\frac{z}{\int_{z_0}^{z_0+z} \exp\{j2\pi f_s[(z'^2 + d^2)^{1/2} - z']\}\mathrm{d}z'}\right|^2. \quad (15)$$

From Fig. 3 it can be seen that the lower the starting point, that is, the nearer the starting point to the focal point of the focusing lens, the larger the value of SIR and the better the performance becomes. It is important to start the vertical scan of the target from the point as close to the focal point as possible.

Next the dependence of the performance on the scanning distance is investigated. Figure 4 shows a plot of three different scanning distances as a function of the starting point of the scans z_0. All other

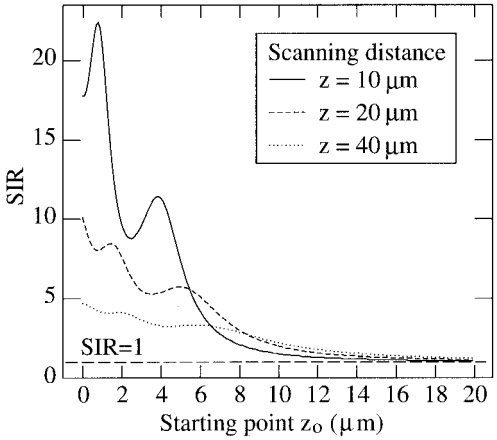

Fig. 4. Performance of the synthetic aperture technique for various scanning distances z at different starting points z_0.

parameters are kept the same as in Fig. 3. Clearly, for small z_0 values, small scanning distances are preferable. However, as the starting point increases, the situation switches; as can be seen from Fig. 4, for $z_0 = 10$ μm the SIR at $z = 40$ μm is better than the other two. For $z_0 = 6$ μm the SIR increases from $z = 10$ μm to $z = 20$ μm, peaking around that value, and decreases when z is further increased. There is a significant dependence in the values of SIR on z and z_0. This is the result from two competing conditions: The increase in scan length provides a longer signal-measuring length for accurate extraction of the base tone f_s; however, as z increases, the field patterns received from the target and from the disturber start to be identical. The Fourier-transform components of the scattered waves from A and B start to be identical, and identification and isolation of the desired signal becomes difficult.

D. Three-Dimensional Laser Microvision with the Synthetic Aperture Approach

Figure 5 shows the complete scanning paths of the synthetic aperture 3-D Laser Microvision. The z-direction scan is for the synthetic aperture processing, and the zigzag scan in the x–y plane is for imaging in lateral directions. At each point in the x–y plane, the synthetic aperture vertical scanning is performed, and the light scattered along the z axis is extracted by use of expression (14). This process is repeated for N wavelength steps, then the FFT is applied to obtain the longitudinal scattering distribution $s(z_m)$. This process is repeated across the x–y plane.

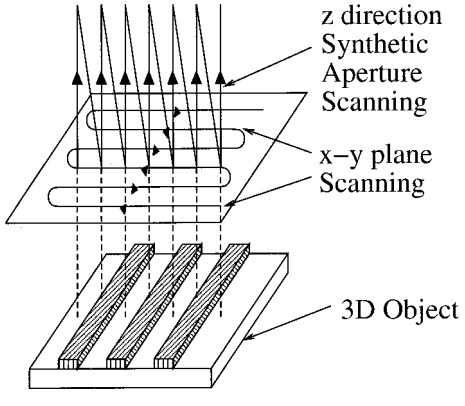

Fig. 5. Scanning paths of the synthetic aperture 3-D Laser Microvision.

This approach removes the lateral resolution dependence on the choice of the objective lens, as it is the synthetic aperture and not the objective lens that provides the lateral resolution. The synthetic aperture 3-D Laser Microvision provides the possibility of fabrication of a lensless high-power microscope with a large depth of focus.

3. Details of the System Layout and Implementation

The system of the 3-D Laser Microvision can be divided broadly into the following three subsystems:

(1) high-resolution digital phase meters,
(2) step frequency light source, and
(3) host and remote computers.

We especially developed points (2) and (3) for our system to process a huge amount of data within a reasonable time. Now we describe each system in detail.

A. High-Resolution Digital Phase Meter

The proposed 3-D Laser Microvision determines the distance from the information of the phase delay of the scattered signal. A specially developed digital phase meter (DPM) can measure the phase angle of the light with an accuracy of 0.03 deg by measuring the phase difference between the returned signal and its reference. It obtains the phase information by measuring the time delay between the rising edge of both signals.

The signal and its reference will first go through a gating circuit in which a pulse window equivalent to the phase delay will be generated. The rising and falling edges of this pulse window will then act, respectively, as the start and stop signals to a subsequent counternetwork. This counternetwork accurately measures the number of clock cycles of a high-frequency clock, running at approximately 1 GHz, that transpire within the time period of the pulse window. A comparison of the measured output count to the calibrated count per full signal period allows the accurate calculation of the desired phase delay.

The DPM excels both in speed and in accuracy when compared with its analog counterpart. First, the DPM requires only three signal periods to complete its acquisition cycle. This is significantly less than an analog phase meter as the integrator located at the mixer output normally requires a much longer time to settle before the analog-to-digital converter can start its measurement. Second, the DPM is less susceptible to noise because it uses only the zero crossing point of the signal to perform its measure-

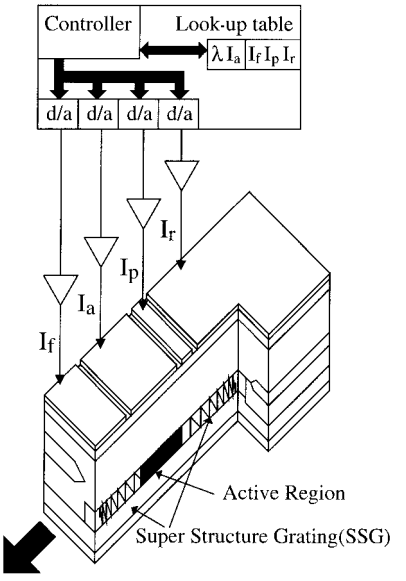

Fig. 6. Schematic drawing of the multiple-phase-shift SSG DBR laser with its current drivers.

ment. The accuracy of the DPM exceeds that of a counterpart analog device by 2 orders of magnitude.

B. Step Frequency Light Source

The SSG DBR laser diode was adopted because no other commercially available light source is fast enough in switching the wavelength in a wide range. This laser covers a range as wide as 30 nm centered at 1.545 μm with an output power of 1 mW. The structure of the SSG DBR laser is shown in Fig. 6. The laser section consists of the front of the SSG, the active phase control, and the rear SSG regions. There is a small difference in the space between the reflection peaks of the front and rear SSG reflectors. The SSG DBR laser diode oscillates at a wavelength where the peaks of the two reflectors match. Because of a Vernier effect, a large tuning range of the laser is achieved even with the limited range in the index of refraction. For one output wavelength, a combination of four bias currents is needed. A look-up table for the bias current was prepared. Each current was provided from the dc current amplifier whose gain is controlled by the digital signal from the remote computer. In practice, this laser is capable of a wavelength stepping time of approximately 2 μs.

C. Host and Remote Computers

To display a 3-D image of an object by the 3-D Laser Microvision, a huge amount of data must be processed. Even to measure one point, the following steps must be executed:

(1) step frequency from $f_0 \ldots f_{N-1}$, typically $N = 128$;
(2) at each frequency step, measure the phase and amplitude of the reflected signal;
(3) perform FFT of the above signal; and
(4) display on the monitor.

For the device to be practical, it is important that the measurement be finished within a reasonable time. To obtain 3-D information the probe beam has to be scanned in a 2-D surface, and at each location the depth information is probed to construct a 3-D image in the end. The total amount of needed information is large. If the sample surface has 128×128 pixels, then there are more than 16,000 pixels. If the measurement of depth takes 1 s at each point on the surface, it would take approximately 4 h to complete the scanning. It is therefore essential to speed up this operation for the device to be practical at all.

To achieve this, all aspects of software and hardware operational efficiency were investigated and utilized to achieve high performance. A dual computer system consisting of a host and remote microcomputers was constructed. Both computers were linked with a Small Computer System Interface (SCSI) to allow bidirectional data transfer. A dedicated digital signal processing (DSP) card was also attached to the host computer for FFT processing. The high-throughput hardware system was accompanied by a software system engineered for speed. Working this system in parallel, we can complete one 3-D image in less than 4 min without synthetic aperture processing.

The normal step frequency radar software design executes a task in a serial manner, running one task after another, waiting for completion of one task before commencing another. In our situation, serial processing imposes one weakness: It puts all the hardware in an idle state most of the time and therefore does not fully utilize the available resources.

Figure 7 illustrates the inefficiencies of serial execution in comparison with parallel execution, which is illustrated in Fig. 8. In the case shown in Fig. 8, five data sets are used, namely, R1 and R2 in the remote computer and H1, H2, and H3 in the host computer. These data sets represent nonoverlapped memory location and can be accessed by the computer or hardware attached to the computer. The trade-off of the execution of tasks in parallel is an increase in memory requirement and an increase in complexity of the software design.

The mechanism depicted in Fig. 8 can be explained easily when we start at the leftmost task. At this time, the remote computer is taking the phase and magnitude of all frequency steps and storing the results in data set R1. In the next time slot, the remote computer will repeat the same task it executed previously, except this time the results will be stored in R2 instead of R1. At the same moment, the SCSI controller in the remote computer will transmit data stored in R1 to the host computer. That is, it is transmitting data that were collected in the previous time slot. Similarly, the host SCSI will receive and store the data in H2. In time slot 3, the remote computer will repeat the same task and store the results back to R1. This means that data collected back in time slot 1 will be overwritten. This is possible because R1 has already transmitted to the host computer. Similarly, remote SCSI will transmit

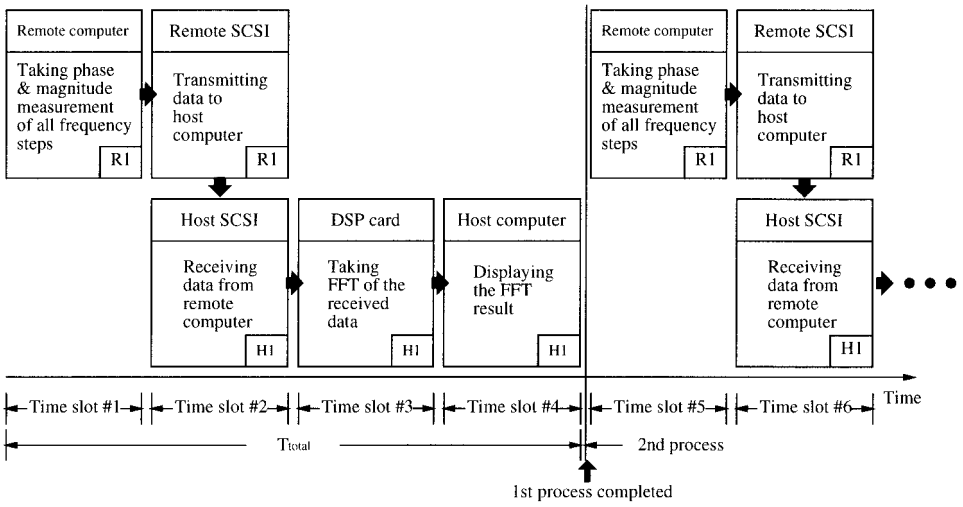

Fig. 7. Task diagram of the processing computer for the case of serial processing.

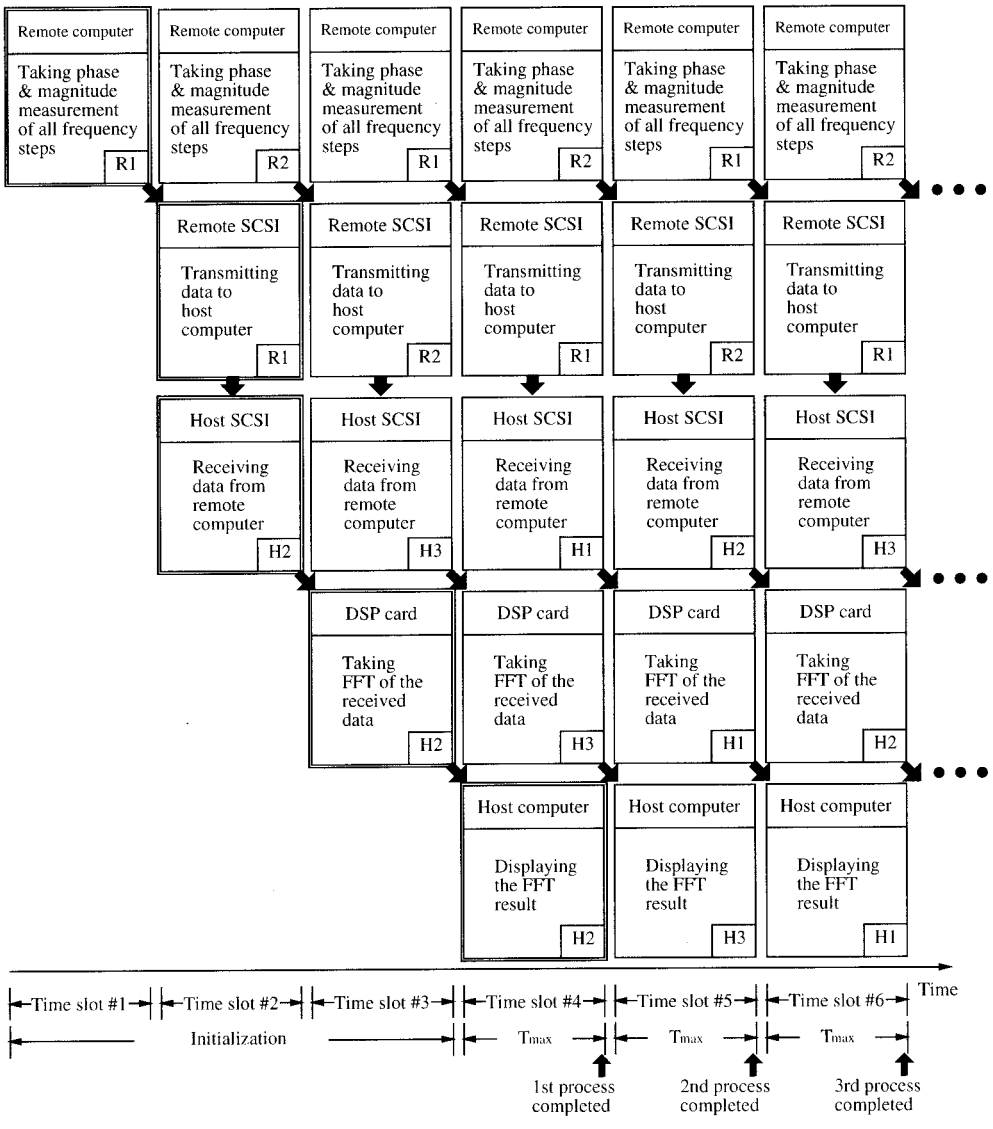

Fig. 8. Same as in Fig. 7, but for the case of parallel processing.

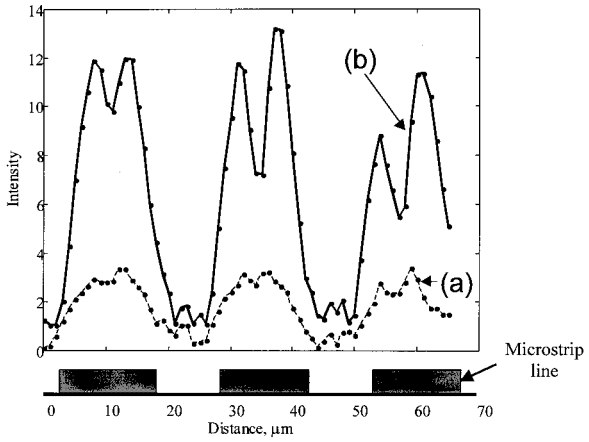

Fig. 9. Measured results: (a) without the synthetic aperture scanning and (b) with the synthetic aperture scanning. The target is an array of microstrip lines at a width of approximately 15 μm whose cross section is shown at the bottom of the figure.

data in R2 to the host SCSI. Data received by the host SCSI will be stored in new location H3. At the same moment, the DSP card will start processing data in H2, and FFT results will be stored back to H2. If one works backward carefully, the DSP card is actually processing data collected by the remote computer back in time slot 1. In this pipelined scheme, all the available resources were efficiently utilized with minimum idle time.

4. Experimental Results

A. Three-Dimensional Laser Microvision with the Synthetic Aperture Approach

We experimentally verified the effectiveness of the synthetic aperture method using a target of a microstrip line array on a GaAs wafer. The drawing at the bottom of Fig. 9 shows the cross section of the element metal strip lines. The width of each microstrip line is 15 μm, the thickness is less than 1 μm, and the spacing between the adjacent edges of the microstrip line is 8 μm. The vertical synthetic aperture was made in the stepwise z direction.

The target used in this evaluation has all its features confined to the surface. In the interest of mitigating the influence of mechanical instabilities over time, we conducted this investigation using a single

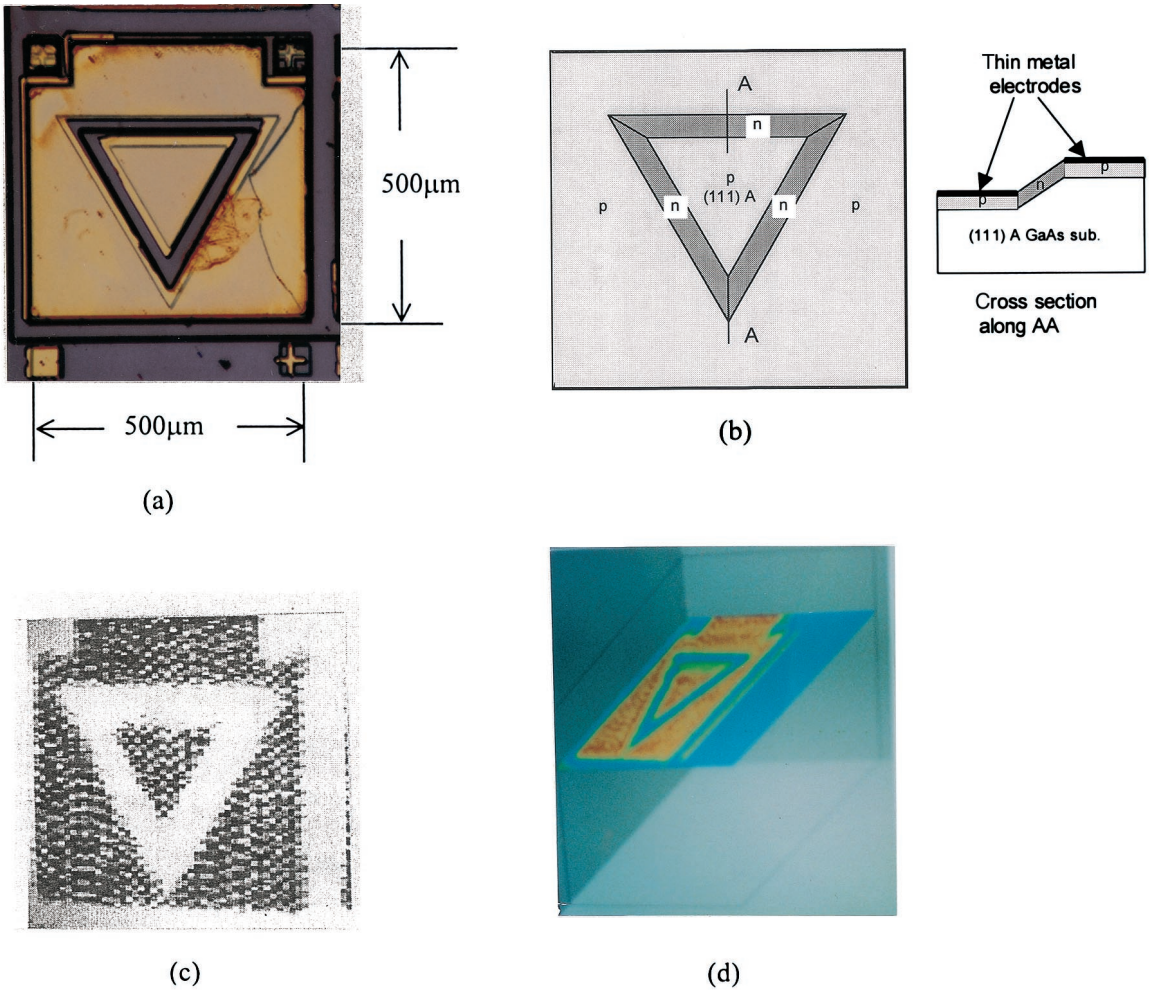

Fig. 10. Displays of the 3-D Laser Microvision. The target was a (111)A GaAs substrate with thin metal electrodes. (a) Photograph of the target, (b) top and cross-sectional view of the target, (c) a quick look of the 2-D display, and (d) 3-D display.

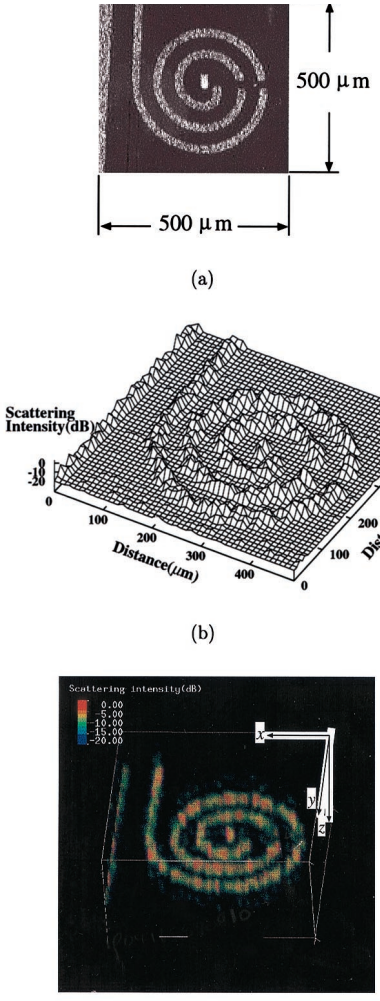

Fig. 11. Images of the microwave IC inductor obtained by the 3-D Laser Microvision. (a) A microwave IC inductor as a target, (b) 2-D scattering intensity of the quick-look display of the target, and (c) 3-D display of the target.

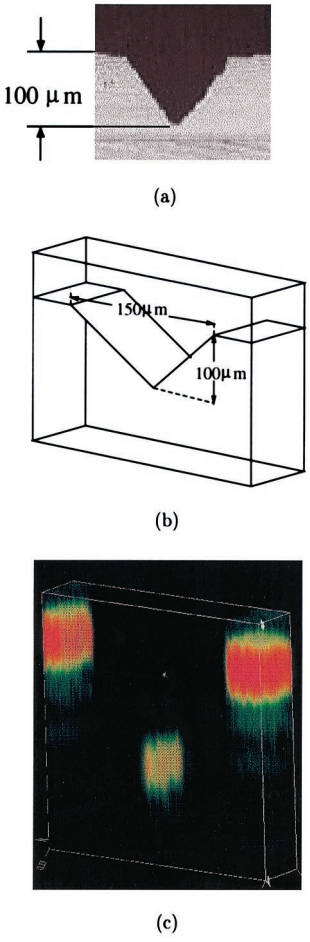

Fig. 12. Image of the V groove. Note that due to the specular reflection, the slanted sides of the groove are not imaged. (a) Photograph of the target, (b) schematic view of the target, and (c) 3-D display of the target.

wavelength of $\lambda = 1.554$ μm, and the sampling grid was covered in approximately 1 min.

We used an objective lens for collecting the light energy but not for focusing the image as such. The image produced when we collected the scattered field at a single height is shown by curve (a) in Fig. 9. It provides a nondefinitive edge of the target. Curve (b) in Fig. 9 shows the result of the synthetic aperture scanning with $z_0 = 5$ μm and $z = 11$ μm, at a step of 0.3 μm. These vertical scans were repeated at every micrometer along the x axis. The image not only clearly separates the edge spacing of the microstrip lines, but also the phenomena of the so-called edge effects of the scattering[18] from the strip are observed, which usually takes place within a few tenths of a wavelength of the illuminating light. The x-axis direction resolution of close to 1 μm was achieved. Thus the focal depth is not restricted by the objective lens, and the image with a large focal depth is obtainable.

B. Some Two- and Three-Dimensional Displays Obtained by the Three-Dimensional Laser Microvision

Figure 10(a) shows a microscope photograph of a tunneling photodiode that is deposited on the (111)A plane of a GaAs substrate. The overall deposit area is 500 μm × 500 μm. The cross-sectional view is shown in Fig. 10(b). The plane view is a triangular shape. The cross section is a trapezoid. The 30-μm-wide terrace is metallized to form an electrode. The dimension of the base is 40 μm. Figure 10(c) shows the 2-D image of a quick-look mode of 32-bit gray-scale 32 × 32 pixels in the x–y plane. The image processing time is fast at the cost of the fine details of the target. The black in the image indicates an area of high reflection, and the white is the area of the low reflection. The background is a thin metal film coating that is highly reflective and hence black. The (111)A GaAs substrate, which is transparent at $\lambda = 1.55$ μm, is white because the least amount of light is reflected. Figure 10(d) shows a 3-D image of the optical tunnel diode. The intensity of reflection is coded.

Figure 11 shows the result when a microwave IC is

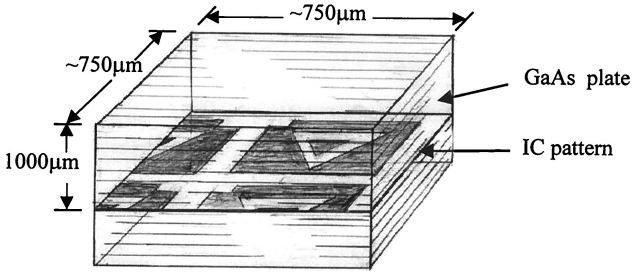

(a)

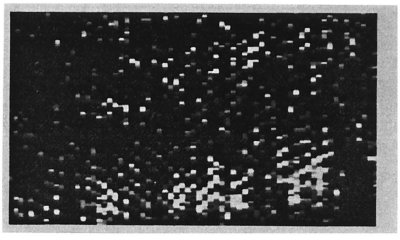

(b)

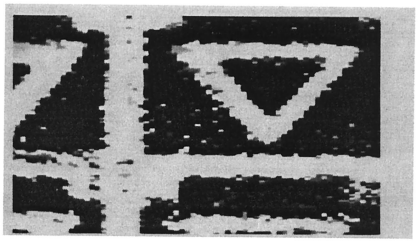

(c)

Fig. 13. 3-D Laser Microvision system pierces through the cover plate and resolves the IC pattern formed within the substrate. (a) Structure of the target: an IC pattern covered by a GaAs plate, (b) image of the top surface of the GaAs cover plate, and (c) image pierced through the cover plate.

used as a target. It is an inductor in an IC form in a microwave circuit. Figure 11(a) is a microscope photograph of the target, and Fig. 11(b) is the measured 2-D scattering intensities of the object. Figure 11(c) shows the 30-μm-wide strip line along with the overpass on the right-hand side of the coil, clearly resolved in the 3-D image obtained by the 3-D Laser Microvision.

The next target is a V groove made on a silicon wafer. Figure 12(a) is a photograph of the side view of the V groove. Figure 12(b) is the schematic layout of the target, and Fig. 12(c) shows the display of the 3-D Laser Microvision. As shown in Fig. 12(a), the slanted sides of the V groove are specular surfaces, and the light does not reflect back toward the detector, except at the bottom of the V groove. This is the reason why the sides of the groove do not appear in the 3-D Laser Microvision display in Fig. 12(c).

Figure 13 demonstrates a see-through capability of the 3-D Laser Microvision. The tunnel photodiode is now covered with a 1-mm-thick sheet of GaAs wafer as shown in Fig. 13(a). Because the GaAs wafer is a

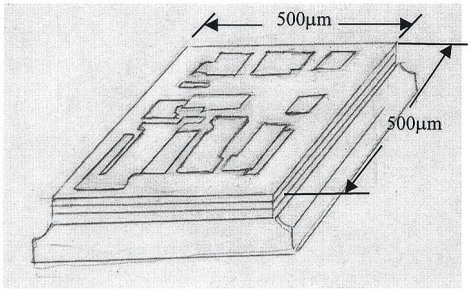

(a)

(b)

Fig. 14. 3-D image taken by the 3-D Laser Microvision. (a) A sketch of the multilayer microwave IC, and (b) 3-D Laser Microvision display resolving the height profile of the target.

dark opaque, the tunneling photodiode pattern cannot be seen by human eyes. Figure 13(b) shows an image obtained by the 3-D Laser Microvision when it sliced at the top surface of the GaAs wafer cover. The index of refraction of GaAs is high with $n = 3.5$, and over 30% of the incident light is reflected from the surface discontinuity. The image shows this reflection. The image is now sliced at the bottom of the cover GaAs wafer. As shown in Fig. 13(c), the details of the tunneling photodiode starts to show up. The see-through capability of the 3-D Laser Microvision is extremely useful as a diagnostic tool for the IC without one having to remove the mold of the chip. In this experiment no synthetic aperture scans in the z direction were employed.

Figure 14(a) is a sketch of a multilayer microwave IC target used to demonstrate the high resolution in the longitudinal direction. Figure 14(b) shows the output from the 3-D Laser Microvision, clearly resolving the small profile features of the IC chip.

5. Conclusion

In this paper we have introduced and demonstrated a new versatile digital imaging tool having a resolution capability of the order of micrometers. Our device can generate 3-D image profiling of targets with a minimum necessity of manipulation. With both the SSG laser diode, which is capable of rapid wavelength switching, and specially developed hardware and software, this device is fully automated and has the capability of interrogating reasonable size targets within a reasonable time. Also, its operation is not

restricted to special environments such as a vacuum. It is also an ideal instrument for measuring the thickness of surfaces even if the surfaces are wet (e.g., coating), as it does not require close proximity and it certainly does not require physical contact. In fact, this device can penetrate through an opaque cover plate, making the device an invaluable apparatus as a metrological tool in the research and development of optical IC's.

References

1. M. K. Barnoski and S. M. Jensen, "Fiber waveguides: a novel technique for investigating attenuation characteristics," Appl. Opt. **15,** 2112–2115 (1976).
2. B. L. Danielson, "Optical time-domain reflectometer specifications and performance testing," Appl. Opt. **24,** 2313–2322 (1985).
3. H. Barfuss and E. Brinkmeyer, "Modified optical frequency domain reflectometry with high spatial resolution," J. Lightwave Technol. **7,** 3–10 (1989).
4. U. Glombitza and E. Brinkmeyer, "Coherent frequency-domain reflectometry for characterization of single-mode integrated-optical waveguides," J. Lightwave Technol. **11,** 1377–1384 (1993).
5. J. Nakayama, K. Iizuka, and J. Nielsen, "Optical fiber fault locator by the step frequency method," Appl. Opt. **26,** 440–443 (1987).
6. K. Iizuka, Y. Imai, A. P. Freundorfer, R. James, R. Wong, and S. Fujii, "Optical step frequency reflectometer," J. Appl. Phys. **68,** 932–936 (1990).
7. R. C. Youngquist, S. Carr, and D. E. N. Davis, "Optical coherence-domain reflectometry; a new optical evaluation technique," Opt. Lett. **12,** 158–160 (1987).
8. K. Hotate and O. Kamatani, "Optical coherence domain reflectometry by synthesis of coherence function," in *Distributed and Multiplexed Fiber Optic Sensors*, A. D. Kersey and J. P. Dakin, eds., Proc. SPIE **1586,** 32–45 (1992).
9. Z. He and K. Hotate, "Measurements for scattering medium by synthesis of optical coherence function with super-structure grating distributed Bragg reflector laser diode," Opt. Rev. **6,** 372–377 (1999).
10. R. E. Lee, *Scanning Electron Microscopy and X-Ray Microanalysis* (Prentice-Hall, New York, 1993).
11. J.-J. Greffet and R. Carminati, "Image formation in near field optics," Prog. Surf. Sci. **56,** 133–237 (1997).
12. P. K. Hansma and J. Tersoff, "Scanning tunneling microscope," J. Appl. Phys. **61,** R1–R23 (1987).
13. M. A. Paesler, *Near Field Optics, Theory, Instrumentation, and Applications* (Wiley, New York, 1996).
14. A. G. Ruiter, J. A. Verman, K. O. van der Werf, and N. F. van Hulst, "Dynamic behavior of tuning fork shear-force feedback," Appl. Phys. Lett. **71,** 28–30 (1997).
15. H. Ishii, F. Kano, Y. Yoshikuni, and H. Yasaka, "Mode stabilization method for superstructure-grating DBR lasers," J. Lightwave Technol. **16,** 433–442 (1998).
16. H. Ishii, H. Tanabe, F. Kano, Y. Tohmori, Y. Kondo, and Y. Yoshikuni, "Quasi-continuous wavelength tuning in super-structure-grating (SSG) DBR lasers," IEEE J. Quantum Electron. **32,** 433–441 (1996).
17. J. W. Goodman, *Introduction to Fourier Optics* (McGraw-Hill, New York, 1968).
18. K. Iizuka and J. L. Yen, "Surface current on triangular and square metal cylinders," IEEE Trans. Antennas Propag. **AP-15,** 795–801 (1967).